



Each performs its own functions: Nickel oxide supported ruthenium single-atoms and nanoclusters relay catalysis with multi-active sites for efficient alkaline hydrogen evolution reaction

Jiachen Zhang, Yanan Gu, Yang Lu, Chengcheng Zhu, Guocong Liu, Chen Wang, Dongmei Sun*, Yawen Tang*, Hanjun Sun*

School of Chemistry and Materials Science, Jiangsu Key Laboratory of New Power Batteries, Jiangsu Collaborative Innovation Centre of Biomedical Functional Materials, Nanjing Normal University, Nanjing 210023, PR China

ARTICLE INFO

Keywords:

Ruthenium
Single-atom catalysts
Multi-active sites
Relay catalysis
Alkaline hydrogen evolution reaction

ABSTRACT

Single-atom catalysts (SACs) have received enormous attention owing to their unique catalytic properties. However, designing SACs for complex reactions with several elementary reactions remains challenging because they commonly accelerate only one step of reactions. Here, the nickel oxide supported ruthenium single-atoms and nanoclusters catalyst ($\text{Ru}_{\text{SA}+\text{NC}}/\text{NiO-NF}$) is reported for the typical multi-step alkaline hydrogen evolution reaction. By altering the ratio of single-atoms/nanoclusters, the synergistic effect between Ru single-atoms and nanoclusters is amplified. The in-situ Raman combined with density functional theory reveals that Ru single-atoms sites display high efficiency on H_2O -adsorption and dissociation, while Ru nanoclusters and NiO sites promote the H-recombination. As a consequence, the prepared $\text{Ru}_{\text{SA}+\text{NC}}/\text{NiO-NF}$ catalyst achieves a low overpotential of 11 mV at a current density of 10 mA cm^{-2} together with a small Tafel slope of $29 \text{ mV decade}^{-1}$. This work offers prospects for the designing of single-atom-based catalysts for multi-step reactions.

1. Introduction

Single-atom catalysts (SACs) are attracting increasing interest in the catalysis field due to the high atom utilization and unique coordination environment, [1–6] resulting in their excellent catalytic activity. However, the single-atom site commonly activated only one step of reactions rather than whole reactions. Thus, their catalytic effect for multi-step reactions consisting of multi-step elementary reactions (e.g. carbon dioxide reduction reaction, oxygen reduction reaction, and hydrogen evolution reaction) is unsatisfactory.[7,8] Therefore, it is vital to construct single-atom-based multi-active sites catalysts to further improve their catalytic activities in multi-step catalytic reactions.

The hydrogen evolution reaction (HER) from electrocatalytic water splitting is regarded as a promising approach for producing hydrogen fuel.[9–12] Meanwhile, The HER is an ideal model reaction for investigating the multi-step catalytic reaction. Specifically, alkaline HER involves the following steps: H_2O -adsorption, H_2O -dissociation, and H-recombination.[13–17] Currently, many efforts have been developed to enhance the catalytic activity of single-atom-based catalysts for HER.

For example, (1) designing dual-single-atoms catalysts (e.g. Co-Pt dual-single-atom catalyst, [18] Co/Se-MoS₂-NF [19]) to optimize the binding energy between the active site and H, (2) constructing single-atom/metal compounds pairs (e.g. $\text{Ru}_1\text{CoP/CDs}$, [20] $\text{Pt}_{\text{SA}}\text{-NiO/Ni}$ [21]) to reduce the energy barrier for H_2O -dissociation. Actually, these above SACs only accelerated individual elementary reactions rather than the whole HER process. For HER multi-step elementary reactions, the rational design of composite catalysts with multi-active sites, where each active site could accelerate one or two steps in the multi-step reactions, rather than just acting as a synergistic site, will benefit to maximize their catalytic activity.

Ruthenium (Ru) has been regarded as a cheaper substitute catalyst (1/3 price of Pt) to Pt owing to its low water dissociation energy barrier for HER [22–24]. Generally, different types of Ru species exhibit different catalytic activities for HER: (1) The electron-deficient Ru single-atom sites (Ru-N, Ru-O) exhibit high efficiency on water dissociation [8,25]. However, they are usually accompanied by poorer H-adsorption capacity. (2) The electron-enriched Ru metallic nanoparticles sites display strong adsorption to H-adsorption, but they hinder

* Corresponding authors.

E-mail addresses: sundongmei@njnu.edu.cn (D. Sun), tangyawen@njnu.edu.cn (Y. Tang), hanjun.sun@njnu.edu.cn (H. Sun).

<https://doi.org/10.1016/j.apcatb.2022.122316>

Received 24 August 2022; Received in revised form 15 November 2022; Accepted 18 December 2022

Available online 20 December 2022

0926-3373/© 2022 Elsevier B.V. All rights reserved.

the H-desorption [26]. Thus, due to their different catalytic mechanisms, a single type of Ru active site is difficult to boost every elementary reaction of the HER process, resulting in a poor catalytic activity. Given this, it is reasonable to design HER electrocatalysts containing multiple active sites, which may accelerate the whole HER process (H_2O -adsorption, H_2O -dissociation, and H-recombination). Here, we attempted to introduce two types of Ru species (Ru single-atoms and Ru nanoclusters) by electrochemical deposition. Since there is an upper limit of single-atoms loading for electrochemical deposition on the [supporting material](#) (influencing factors: vacancies, edges, steps etc), [27] the ratio of single-atoms/nanoclusters can be precisely modulated by changing the concentration of the RuCl_3 electrolyte. Given this, we designed an electrocatalyst composed of Ru single-atoms and nanoclusters supported on the NiO nanosheet ($\text{Ru}_{\text{SA+NC}}/\text{NiO-NF}$). Combining the in-situ Raman and density functional theory (DFT), we postulated that the existence of Ru single-atoms coordinated with O groups (Ru-O_4) on the NiO matrix displayed high efficiency on water adsorption and dissociation, while the Ru nanoclusters promoted the adsorption of H. Moreover, owing to weak binding energy between NiO and H, the adsorbed H migrated from the Ru nanoclusters sites to NiO sites through H spillover and desorbed from NiO sites. Due to the different characteristics of Ru single-atoms sites, Ru nanoclusters sites, and NiO sites, the $\text{Ru}_{\text{SA+NC}}/\text{NiO-NF}$ accelerated each reaction step through relay catalysis during the whole HER process. As expected, the as-prepared $\text{Ru}_{\text{SA+NC}}/\text{NiO-NF}$ catalyst displayed a low overpotential at 10 mA cm^{-2} (11 mV) and a low Tafel slope of 29 mV dec^{-1} in 1.0 M KOH electrolyte, which was much lower than those of commercial Pt/C (21 mV at 10 mA cm^{-2} , Tafel slope of 32 mV dec^{-1}) and other recently reported Pt-based and Ru-based HER electrocatalysts. This work mechanistically reveals the synergetic effect of a composite catalyst with multiple active sites and provides a new design strategy for catalyzing multistep reactions.

2. Experimental sections

2.1. Materials

Nickel(II) nitrate hexahydrate ($\text{Ni}(\text{NO}_3)_2 \cdot 6 \text{ H}_2\text{O}$), Urea ($\text{CO}(\text{NH}_2)_2$), Ammonium fluoride (NH_4F) and Potassium hydroxide (KOH) were purchased from Sinopharm Chemical Reagent Co., Ltd (Shanghai, China). Ruthenium (III) chloride hydrate ($\text{RuCl}_3 \cdot x\text{H}_2\text{O}$) was purchased from DB Biotechnology Co., Ltd. (Shanghai, China). All the reagents were of analytical grade and used as received without further purification. Deionized water was used throughout the experimental processes.

2.2. Preparation of $\text{Ni}(\text{OH})_2\text{-NF}$

First, the Ni foam was successively washed with acetone, ethanol, 2 M HNO_3 aqueous solution, and deionized water. Second, one piece of nickel foam ($2 \times 4 \text{ cm}^2$) was immersed into a 30 mL water solution containing $1.24 \text{ mmol Ni}(\text{NO}_3)_2 \cdot 6 \text{ H}_2\text{O}$, $2.50 \text{ mmol NH}_4\text{F}$, and $6.00 \text{ mmol CO}(\text{NH}_2)_2$ in a Teflon autoclave (Anhui Kemi Machinery Technology Co., Ltd) and then was heated for 8 h at 160°C . After cooling to room temperature, the product was washed with deionized water and dried at 40°C .

2.3. Preparation of $\text{Ru}_{\text{SA+NC}}/\text{NiO-NF}$

In a typical synthesis, $\text{Ru}_{\text{SA+NC}}/\text{NiO-NF}$ was fabricated by electro-deposition approach. The Ru loading on $\text{Ni}(\text{OH})_2\text{-NF}$ was carried out with a three-electrode system using $\text{Ni}(\text{OH})_2\text{-NF}$ ($2 \times 2 \text{ cm}^2$) as the working electrode, a graphite plate as the counter electrode, and a saturated calomel electrode (SCE) as the reference electrode. The electrochemical deposition process was carried out at -1.0 V vs SCE for 1 h in 0.02 M RuCl_3 electrolyte. After deposition, the sample was annealed at 350°C in argon for 3 h to form $\text{Ru}_{\text{SA+NC}}/\text{NiO-NF}$. The same procedure was also adopted for the synthesis of $\text{Ru}/\text{NiO-NF}$ with different Ru

contents by changing the concentration of RuCl_3 electrolyte ($0.01\text{--}0.05 \text{ M}$).

2.4. Preparation of NiO-NF

NiO-NF was prepared from $\text{Ni}(\text{OH})_2\text{-NF}$ by annealing at 350°C in argon for 3 h .

2.5. Characterization

The crystal structure information of the as-fabricated samples was measured by X-ray powder diffraction (XRD) on a D/max-rC X-ray diffractometer (Cu $\text{K}\alpha$ radiation, $\lambda = 1.5406 \text{ \AA}$). Elemental mapping images and HAADF-STEM images were performed on a FEI Tecnai G2 F20 microscope, an accessory built on the JEOL JEM-2100 F. X-ray photoelectron spectroscopy (XPS) was examined by Thermo VG Scientific ESCALAB 250 spectrometer with an Al $\text{K}\alpha$ light source. The X-ray absorption spectra (XAS) including X-ray absorption near-edge structure (XANES) and extended X-ray absorption fine structure (EXAFS) of the samples at Ru K -edge were collected at the Singapore Synchrotron Light Source (SSLS) center, where a pair of channel-cut Si (111) crystals was used in the monochromator, the Ru K -edge XANES data were recorded in a transmission mode. Ru foil and RuO_2 were used as references. The storage ring was working at the energy of 2.5 GeV with an average electron current of below 200 mA . The acquired EXAFS data were extracted and processed according to the standard procedures using to ATHENA module implemented in the FEFFIT software packages. In-situ Raman spectra were measured with a Finder One Raman spectrometer (Zolix, China). A 638 nm solid-state laser with an exact power of 10 mW was used as the excitation source. Calibration was performed using a silicon wafer standard (520 cm^{-1}). Before each experiment, the intensity and laser wavelength were calibrated using a polished silicon wafer. The measured potential range was from $+0.20\text{--}0.00 \text{ V}$ vs RHE with a potential gap of 0.05 V . All the electrochemical tests were performed in 1.0 M KOH electrolyte.

2.6. Electrocatalytic HER measurement

Electrocatalytic hydrogen production test in 1.0 M KOH : The electrocatalytic hydrogen production (HER) test adopts a three-electrode test system and is equipped with a Shanghai Chenhua Instrument Co., Ltd. electrochemical workstation model CHI760E to evaluate its catalytic activity. For electrode preparation, the catalysts were cut into a piece of $1 \times 1 \text{ cm}^2$ and used as the working electrode. A standard Hg/HgO (1.0 M KOH) electrode and a graphite rod were used as the reference and counter electrode, respectively. The measured current density (j) was obtained by the equation: $j = \text{current (I)} / \text{disk area (S)}$.

2.7. Calculation of the total turnover frequency (TOF)

The TOF (in s^{-1}) reported in this work is an apparent TOF value based on the number of metal atoms in catalyst, which was calculated with the following equation:

$$\text{TOF} = \frac{I}{2NF}$$

I: current (A) during the linear sweep voltammetry (LSV) tests in 1.0 M KOH .

N: Number of active sites (in mol).

F: Faraday constant (96485.3 C/mol).

The factor $1/2$ arrives by taking into account that two electrons are required to form one hydrogen molecule from two protons.

The CV measurements of the freshly prepared $\text{Ru}_{\text{SA+NC}}/\text{NiO-NF}$ and Pt/C electrodes were carried out in PBS electrolyte (pH 7) to quantify the number of active sites. Assuming a one-electron redox process, the number of active sites (n) of these catalysts was calculated from the

following equation: $n = Q/2F$, where F and Q are the Faraday constant and the whole charge of the CV curve, respectively.

2.8. DFT computations

The density functional theory (DFT) calculations were performed with the VASP package. Zero damping D3 correction method of Grimme was used to describe van der Waals interactions. Built to the vacuum layer spacing was set to 15 Å along the z direction to avoid interactions between periodic images. The generalized gradient approximation (GGA) of Perdew-Burke-Ernzerhof (PBE) was used to calculate exchange-correlation energies, where the force-, energy-convergence criterion for self-consistent field (SCF), and energy cutoff were set to 1×10^{-5} eV, 0.05 eV Å⁻¹, and 450 eV, respectively. A Monkhorst–Pack ($3 \times 3 \times 1$) k -point grid was employed for faster convergence during optimization. Free energy diagrams for HER were computed using a computational hydrogen electrode (CHE) model, which suggests that the

chemical potential of a proton/electron ($H^+ + e^-$) is equal to half of that of one H_2 gas molecule. The change in free energy (ΔG) for each step in the overall transformation was determined using the following equation, " $\Delta G = \Delta E + \Delta ZPE - T\Delta S$ ", where ΔE , ΔZPE , and ΔS are the differences in the total energies, zero-point energies, and entropies between the reactant and product, respectively. The zero-point energy values reported by Nørskov et al. were used for all reaction steps, and ΔS was taken from thermodynamic tables at $T = 298$ K.

3. Results and discussion

3.1. Material synthesis and characterization

Fig. 1a displayed the schematic preparation process of NiO nanosheet supported Ru single-atoms and Ru nanoclusters on nickel foam. Firstly, the $Ni(OH)_2$ nanosheet array on nickel foam (denoted as $Ni(OH)_2/NF$) was prepared through a hydrothermal process. The X-ray

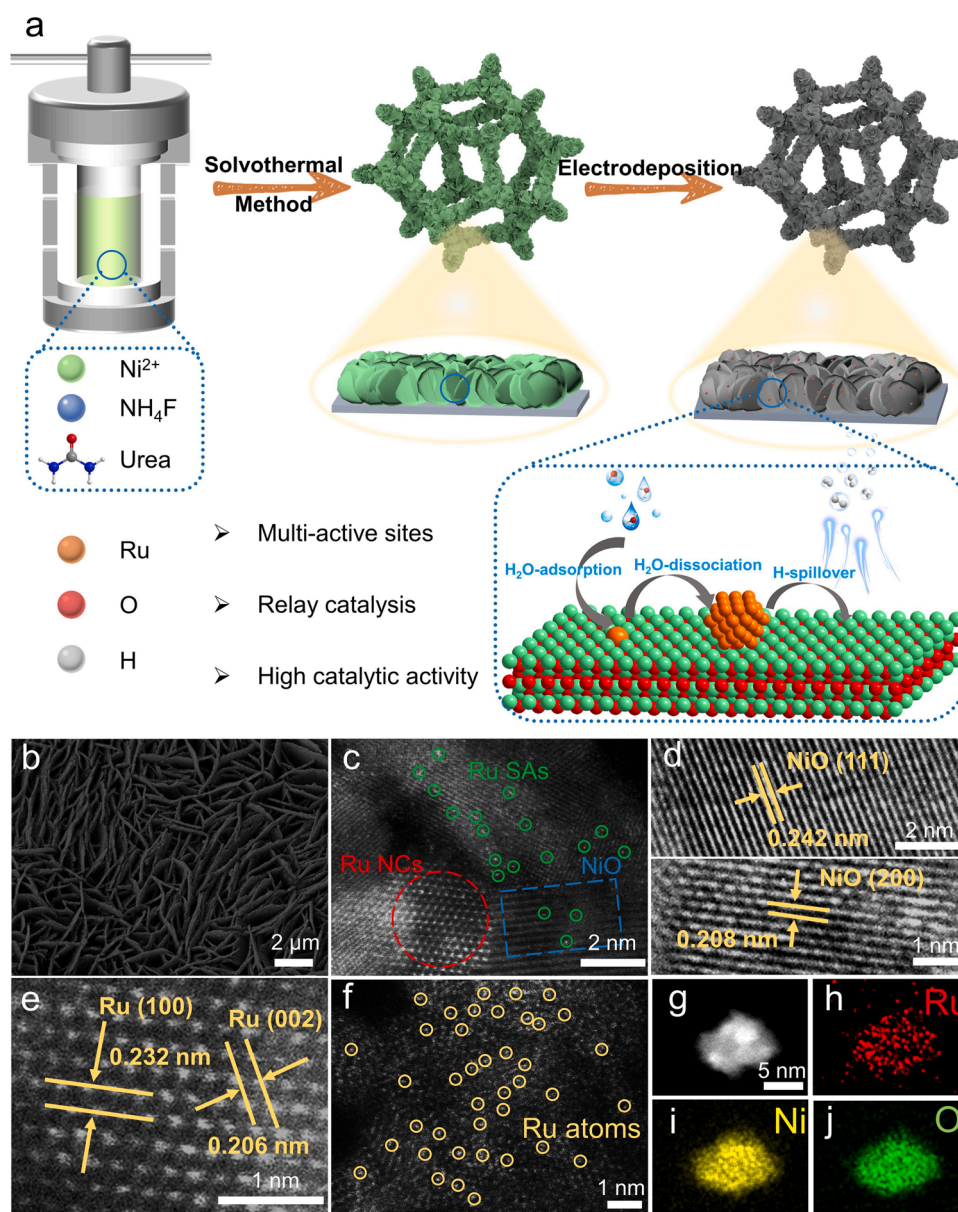


Fig. 1. (a) Schematic synthesis and structural characterizations of $Ru_{SA+NC}/NiO-NF$. (b) SEM images of $Ru_{SA+NC}/NiO-NF$. (c-f) HAADF-STEM images of $Ru_{SA+NC}/NiO-NF$, confirming the co-existence of Ru single-atoms and Ru nanoclusters and NiO; (g-j) HAADF-STEM images of the $Ru_{SA+NC}/NiO-NF$ and corresponding elemental distribution maps of Ni, Ru, and O in the $Ru_{SA+NC}/NiO-NF$.

diffraction (XRD) measurement demonstrated that the main diffraction peaks of the $\text{Ni}(\text{OH})_2/\text{NF}$ (Fig. S1, Supporting Information) was well indexed to the nickel hydroxide (JCPDS No. 73–1520). Then the Ru species anchoring on the surface of $\text{Ni}(\text{OH})_2/\text{NF}$ were fabricated via the electrochemical deposition in 0.02 M RuCl_3 electrolyte (denoted as $\text{Ru}/\text{Ni}(\text{OH})_2\text{-NF}$). After annealing at 350 °C in the Ar atmosphere, the $\text{Ni}(\text{OH})_2$ was transformed to NiO (Fig. S2). As shown in the Fig. 1b, numerous uniform distributed and interconnected nanosheets were observed on the nickel foam (lateral size of 0.9–1.2 μm and a thickness of 50–85 nm) by scanning electron microscopy (SEM), which were similar with those of the $\text{Ni}(\text{OH})_2$ and NiO nanosheets on NF (Figs. S3–4, Supporting Information), indicating that the structure of the obtained catalyst kept unchanged after the electrochemical deposition and calcination. Meanwhile, high-angle annular dark field scanning transmission electron microscopy (HAADF-STEM) were applied to identify Ru species on the surface of NiO nanosheet. As displayed in Fig. 1c–f, the lattice fringes with the spacing of 0.242 nm and 0.208 nm corresponded to the (111) and (200) planes of NiO ; the lattice distance of 0.232 nm and 0.206 nm were assigned to the Ru (100) and Ru (002), respectively. Markedly, abundant atomically dispersed Ru atoms (bright dots) and Ru nanoclusters (1–3 nm, highlighted with yellow circles) were clearly observed on the NiO nanosheet, which demonstrated that two types of Ru species were successfully synthesized on the surface of NiO nanosheet. The energy dispersive X-ray spectroscopy (EDS) elemental

mapping analysis further revealed the uniform distribution of Ru, Ni, and O (Fig. 1g–j). Obviously, no diffraction peaks related to Ru species were detected by the XRD patterns, which can be attributed to the low Ru content (0.37 wt% for $\text{Ru}_{\text{SA+NC}}/\text{NiO-NF}$ examined by the inductively coupled plasma). In addition, the $\text{Ru}/\text{NiO-NF}$ with different Ru contents were prepared by changing the concentration (0.01–0.05 M) of the RuCl_3 electrolyte. XRD and SEM were also carried out to explore their components and morphologies, the results showed that all the RuNiO-NF exhibited similar structure and composites (Fig. S5–7, Supporting Information).

To unravel the chemical composition and electronic properties of $\text{Ru}_{\text{SA+NC}}/\text{NiO-NF}$, X-ray photoelectron spectroscopy (XPS) was conducted. For the $\text{Ru}_{\text{SA+NC}}/\text{NiO-NF}$, the peak located at 854.2 and 873.6 eV with two shakeup satellites (861.0 and 879.2 eV) were assigned to $\text{Ni } 2p_{3/2}$ and $\text{Ni } 2p_{1/2}$. Among them, the singal peaks at 855.3 and 873.1 eV were attributed to Ni^{2+} species, and the other two peaks centered at 853.8 and 871.4 eV were associated with the Ni^0 (Fig. S8, Supporting Information). In Ru 3p spectra, the peaks located at 463.0 and 485.1 eV were attributed to the metallic Ru^0 and single-atom Ru^{x+} species, the Ru single-atom with positive valence can also be confirmed by the X-ray absorption of fine structure (XAFS) [19,28,29]. Meanwhile, the O 1s spectra can be deconvoluted into two peaks, the signal peaks at 529.2 and 530.6 eV were assigned to the Ni (Ru)-O and physically/chemically adsorbed water species, respectively [8]. In

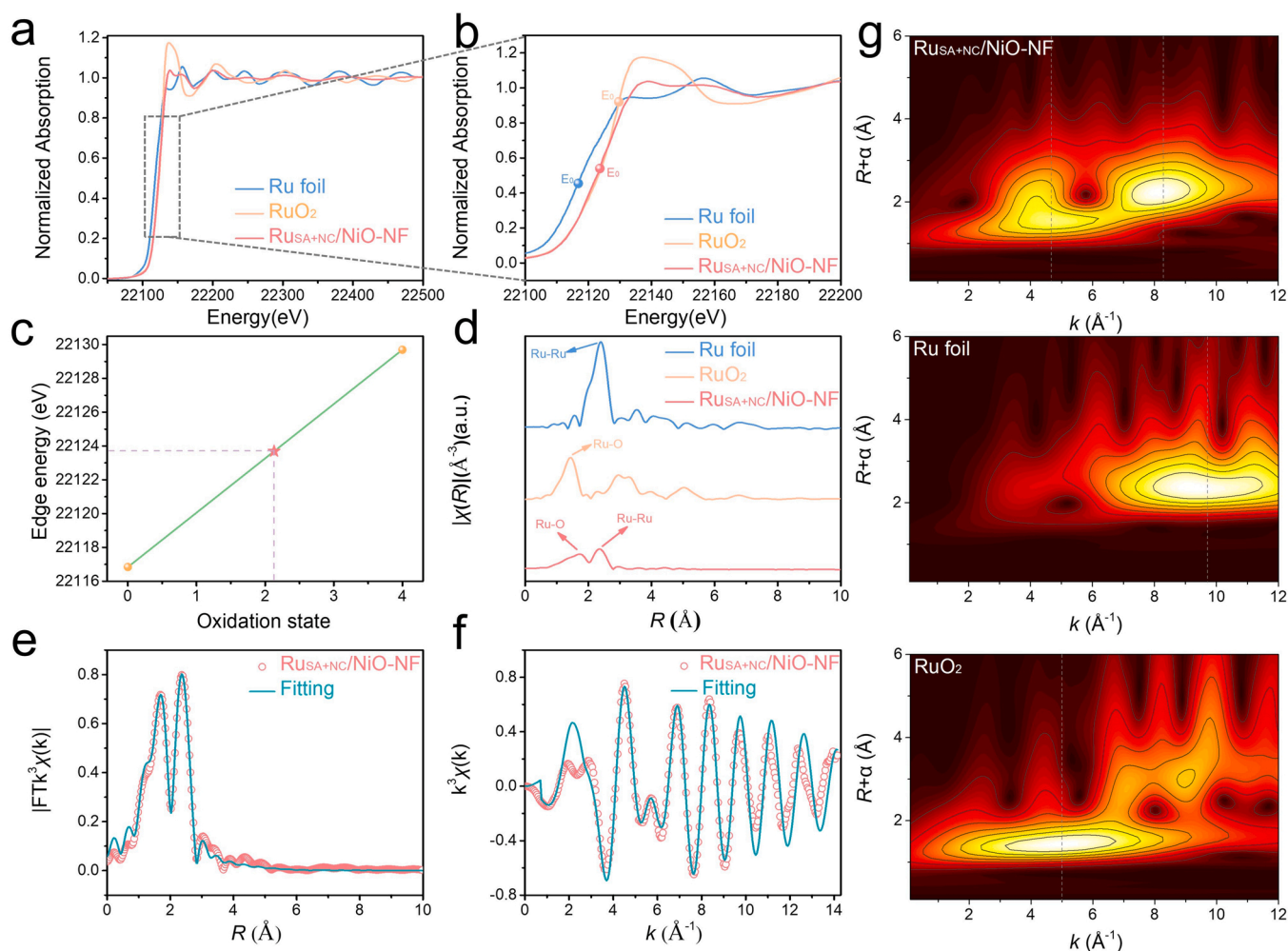


Fig. 2. (a) Ru K-edge XANES spectra of $\text{Ru}_{\text{SA+NC}}/\text{NiO-NF}$, Ru foil, and RuO_2 ; (b) Ru K-edge with different absorption energy (E_0) for $\text{Ru}_{\text{SA+NC}}/\text{NiO-NF}$, Ru foil, and RuO_2 , respectively; (c) Relationship between Ru K-edge absorption energy (E_0) and oxidation state for $\text{Ru}_{\text{SA+NC}}/\text{NiO-NF}$; (d) Fourier-transformed Ru K-edge EXAFS spectra of $\text{Ru}_{\text{SA+NC}}/\text{NiO-NF}$, Ru foil, and RuO_2 ; EXAFS fitting curves of $\text{Ru}_{\text{SA+NC}}/\text{NiO-NF}$ at the (e) R space and (f) K space; (g) Wavelet transforms for the k^3 -weighted Ru K-edge EXAFS signals of $\text{Ru}_{\text{SA+NC}}/\text{NiO-NF}$, Ru foil, and RuO_2 , respectively.

comparison of those of NiO-NF (Fig. S9-10, Supporting Information), the binding energies of Ni in $\text{Ru}_{\text{SA+NC}}/\text{NiO-NF}$ had slight negative shifts of 0.9 eV, indicating the strong interaction between Ru atoms and NiO changed the charge density of Ni [19]. In addition, the $\text{Ru}^{x+}/\text{Ru}^0$ ratios of Ru/NiO-NF with different Ru content were also analyzed (Fig. S11). The binding energies of Ru 3p in all Ru/NiO-NF samples were between Ru (0) 3p and Ru (IV) 3p, [30] demonstrating that the Ru oxidation state in Ru/NiO-NF was between 0 and + 4. Meanwhile, with the increasing concentration of the RuCl_3 electrolyte (0.01–0.05 M) during electrodeposition, the $\text{Ru}^{x+}/\text{Ru}^0$ ratio for Ru/NiO-NF was changed from 1.20 to 0.76, indicating that more nanoclusters were generated (Fig. S11). [27].

The XAFS was used to unveil the electronic structure and coordination environment of Ru species on $\text{Ru}_{\text{SA+NC}}/\text{NiO-NF}$. Fig. 2a displayed the X-ray absorption near edges structure (XANES) of the Ru K-edge region of the $\text{Ru}_{\text{SA+NC}}/\text{NiO-NF}$, the Ru foil and RuO_2 were also measured as the references. The partially enlarged illustration (Fig. 2b) showed the threshold value (E_0) of $\text{Ru}_{\text{SA+NC}}/\text{NiO-NF}$ (22123.68 eV) was between Ru foil (22116.83 eV) and RuO_2 (22129.69 eV), suggesting the transition energy from 1 s to the outermost shell orbitals in these three samples increased in the order: Ru foil < $\text{Ru}_{\text{SA+NC}}/\text{NiO-NF}$ < RuO_2 . The enhanced transition energy can be attributed to the formation of Ru-O bonds, which owned strong dipole hybridization and pushed up the empty 5d orbitals. [31] To evaluate the oxidation state of Ru in $\text{Ru}_{\text{SA+NC}}/\text{NiO-NF}$, E_0 was used as the function of the oxidation state of Ru in these three materials. [32] Here, the average Ru oxidation state in $\text{Ru}_{\text{SA+NC}}/\text{NiO-NF}$ was + 2.1 (Fig. 2c), which was well consistent with the XPS analysis. The Fourier-transformed extended X-ray absorption fine structure (FT-EXAFS) of $\text{Ru}_{\text{SA+NC}}/\text{NiO-NF}$ presented two distinct peaks at 1.72 Å and 2.35 Å, respectively (Fig. 2d). The peak at 1.72 Å was attributed to the Ru-O bond of atomic Ru coordinated with O in the NiO substrate, which was different from that of RuO_2 (1.42 Å). And another characteristic peak (3.15 Å) for RuO_2 was not observed in the EXAFS

spectrum of $\text{Ru}_{\text{SA+NC}}/\text{NiO-NF}$, indicating the absence of RuO_2 in $\text{Ru}_{\text{SA+NC}}/\text{NiO-NF}$. The peak at 2.35 Å was associated with the Ru-Ru bond, demonstrating the presence of Ru nanoclusters. Then the quantitative EXAFS curve-fitting analyses for $\text{Ru}_{\text{SA+NC}}/\text{NiO-NF}$ exhibited the coordination number of Ru-O bonding was ≈ 4.1 , demonstrating the formation of Ru-O₄ coordination structure (Fig. 2e-f, Table S1). Furthermore, the wavelet transforms (WT) of the EXAFS spectrum showed two signal peaks at 4.66 Å⁻¹ and 8.28 Å⁻¹. By comparing the spectrum of Ru foil and RuO_2 , we concluded that the signal peaks were associated with the Ru-O and Ru-Ru scattering path, further verifying the co-existence of Ru single-atoms and Ru nanoclusters (Fig. 2g).

3.2. HER performance of $\text{Ru}_{\text{SA+NC}}/\text{NiO-NF}$

The HER performance of $\text{Ru}_{\text{SA+NC}}/\text{NiO-NF}$ was evaluated in N₂-saturated 1.0 M KOH solution with a typical three-electrode system. The linear sweep voltammetry (LSV) curves were iR-corrected in this work and all the potentials were referenced to the reversible hydrogen electrode (RHE). For comparison, the HER performance of commercial Pt/C (20%), Ru/C (20%), NiO-NF, and bare NF were also measured under the same test conditions. As shown in Fig. 3a, NiO-NF performed poor activity with an overpotential of 192 mV to reach the current density of 10 mA cm⁻². After the introduction of Ru species, the $\text{Ru}_{\text{SA+NC}}/\text{NiO-NF}$ displayed a near zero onset overpotential. Moreover, the $\text{Ru}_{\text{SA+NC}}/\text{NiO-NF}$ only needed a low overpotential of 11 mV to reach the current density of 10 mA cm⁻², which was lower than that of commercial Pt/C (22 mV @ 10 mA cm⁻²) and Ru/C (101 mV @ 10 mA cm⁻²). The Tafel slopes derived from the LSV curves could also be demonstrated its outstanding catalytic activity, which is an important indicator to access the reaction kinetics. The $\text{Ru}_{\text{SA+NC}}/\text{NiO-NF}$ displayed a Tafel slope of 29.2 mV dec⁻¹, which was smaller than that of Pt/C (34.3 mV dec⁻¹), Ru/C (76.6 mV dec⁻¹), and NiO-NF (82.3 mV dec⁻¹), demonstrating the

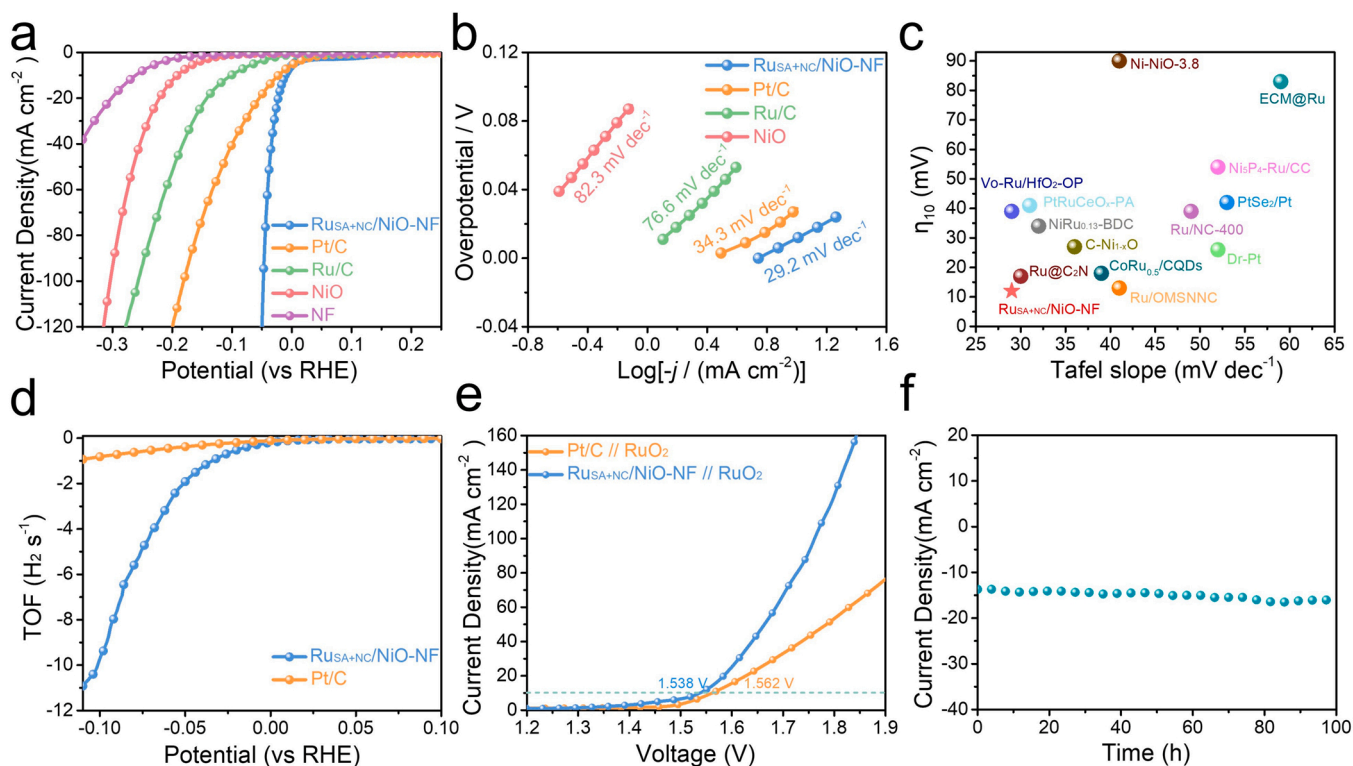


Fig. 3. (a) The HER polarization curves (iR compensated) and (b) the corresponding Tafel plots LSV curves of $\text{Ru}_{\text{SA+NC}}/\text{NiO-NF}$, Ru/C (20%), Pt/C (20%), NiO-NF, and NF. (c) Comparison with the recently reported Ru-based, Ni-based, and Pt-based HER electrocatalysts in 1.0 M KOH. (d) Calculated TOFs of $\text{Ru}_{\text{SA+NC}}/\text{NiO-NF}$ and Pt/C (20%) in 1.0 M KOH. (e) Polarization curves (iR compensated) of the $\text{Ru}_{\text{SA+NC}}/\text{NiO-NF} // \text{RuO}_2$ and Pt/C // RuO_2 couple for overall water splitting. (f) Long-term stability tests of $\text{Ru}_{\text{SA+NC}}/\text{NiO-NF}$.

reaction pathways follow the Volmer-Tafel mechanism (Fig. 3b). By tuning the $\text{Ru}^{x+}/\text{Ru}^0$ ratios of $\text{Ru}/\text{NiO-NF}$, the catalytic activity could be optimized. As shown in Fig. S12 and Table S2, when the concentration of the RuCl_3 electrolyte was 0.02 M, the $\text{Ru}/\text{NiO-NF-0.02}$ displayed the minimum overpotential (11 mV @ 10 mA cm^{-2}) and Tafel slope (29 mV dec^{-1}), which was much lower than those of $\text{Ru}/\text{NiO-NF-0.01}$ (overpotential at 10 mA cm^{-2} : 32 mV; Tafel slope: 47 mV dec^{-1}) and $\text{Ru}/\text{NiO-NF-0.05}$ (overpotential at 10 mA cm^{-2} : 23 mV; Tafel slope: 36 mV dec^{-1}). Furthermore, the exchange current density (j_0) was also calculated by extrapolating the Tafel plot (Fig. S13, Supporting Information), the j_0 of $\text{Ru}_{\text{SA+NC}}/\text{NiO-NF}$ was 5.89 mA cm^{-2} , which was better than that of Pt/C (3.42 mA cm^{-2}), Ru/C (0.94 mA cm^{-2}) and NiO-NF (0.11 mA cm^{-2}), reflecting the faster kinetics than other catalysts in this work. In addition, the HER activity of $\text{Ru}_{\text{SA+NC}}/\text{NiO-NF}$ was also better than most recent reported Pt-based, Ru-based and Ni-based catalysts (Fig. 3c; Table S3, Supporting Information), such as PtNi-O/C ($\approx 42 \text{ mV}$ at 10 mA cm^{-2}), [33] Dr-Pt ($\approx 26 \text{ mV}$ at 10 mA cm^{-2}), [34] $\text{CoRu}_{0.5}/\text{CQDs}$ ($\approx 18 \text{ mV}$ at 10 mA cm^{-2}), [35] $\text{NiRu}_{0.13}\text{-BDC}$ ($\approx 36 \text{ mV}$ at 10 mA cm^{-2}), [36] $\text{C-Ni}_{1-x}\text{O}$ ($\approx 27 \text{ mV}$ at 10 mA cm^{-2}), [37] $\text{Ni}/\text{NiO-3.8}$ ($\approx 90 \text{ mV}$ at 10 mA cm^{-2}) (Fig. 3c) [38].

The turnover frequency (TOF) was calculated to measure the intrinsic catalytic activity of different catalysts (Fig. 3d; Fig. S14, Supporting Information), the TOF value of $\text{Ru}_{\text{SA+NC}}/\text{NiO-NF}$ was 1.91 s^{-1} at the overpotential of 50 mV, which was ~ 5 times higher than that of commercial Pt/C (0.51 s^{-1}), and even outperformed most reported catalysts, including Ru@MWCNT (0.4 s^{-1} at 25 mV), [39] RuCo ANSs (8.52 s^{-1} at 100 mV), [40] $\text{Ru}/\text{Ni}_3\text{V-LDH}$ (3.5 s^{-1} at 100 mV), [41] $\text{Ru}_1/\text{D-NiFe LDH}$ (7.66 s^{-1} at 100 mV) [42]. The double-layer capacitance (C_{dl}) was calculated to estimate the electrochemical surface areas (ECSA). The C_{dl} of $\text{Ru}_{\text{SA+NC}}/\text{NiO-NF}$ was 24.5 mF cm^{-2} , which was much

higher than that of NiO-NF (2.1 mF cm^{-2}), indicating that $\text{Ru}_{\text{SA+NC}}/\text{NiO-NF}$ possessed more accessible active sites (Fig. S15, Supporting Information). Moreover, the Faradaic efficiency (FE) of $\text{Ru}_{\text{SA+NC}}/\text{NiO-NF}$ was measured by the water drainage method, which was close to 100% during the real water splitting (Fig. S16, Supporting Information). Owing to its superior HER activity, an alkaline electrolyzer was assembled using $\text{Ru}_{\text{SA+NC}}/\text{NiO-NF}$ as cathode and commercial RuO_2 as anode. As shown in Fig. 3e, the $\text{Ru}_{\text{SA+NC}}/\text{NiO-NF} // \text{RuO}_2$ couple required 1.538 V and 1.664 V to achieve a current density of 10 and 50 mA cm^{-2} , which was better than that of $\text{Pt/C} // \text{RuO}_2$ couple (1.562 V @ 10 mA cm^{-2} , 1.785 V @ 50 mA cm^{-2}).

Since stability is a crucial criterion to evaluate the catalytic activity, [43] the electrocatalytic stability of the $\text{Ru}_{\text{SA+NC}}/\text{NiO-NF}$ was evaluated by the chronoamperometry test. As shown in Fig. 3f, the current density was maintained well after the long-term electrolysis for 100 h, indicating excellent catalytic stability. In contrast, the current density of Pt/C was only maintained 63% after 25 h (Fig. S17, Supporting Information). Additionally, the $\text{Ru}_{\text{SA+NC}}/\text{NiO-NF} // \text{RuO}_2$ couple also exhibited a superior durability, no obvious degradation of current density was found after 25 h, manifesting great potential in the application for industrial overall water splitting (Fig. S18, Supporting Information). In addition, the SEM images of NiO-NF showed that nanosheet morphology maintained well after durability tests (Fig. S19, Supporting Information). The XRD and XPS pattern also demonstrated that the structure of $\text{Ru}_{\text{SA+NC}}/\text{NiO-NF}$ had no obvious change (Fig. S20-21, Supporting Information).

4. Understanding the active sites of $\text{Ru}_{\text{SA+NC}}/\text{NiO-NF}$

To explore the origin of excellent HER performance of $\text{Ru}_{\text{SA+NC}}/\text{NiO-NF}$

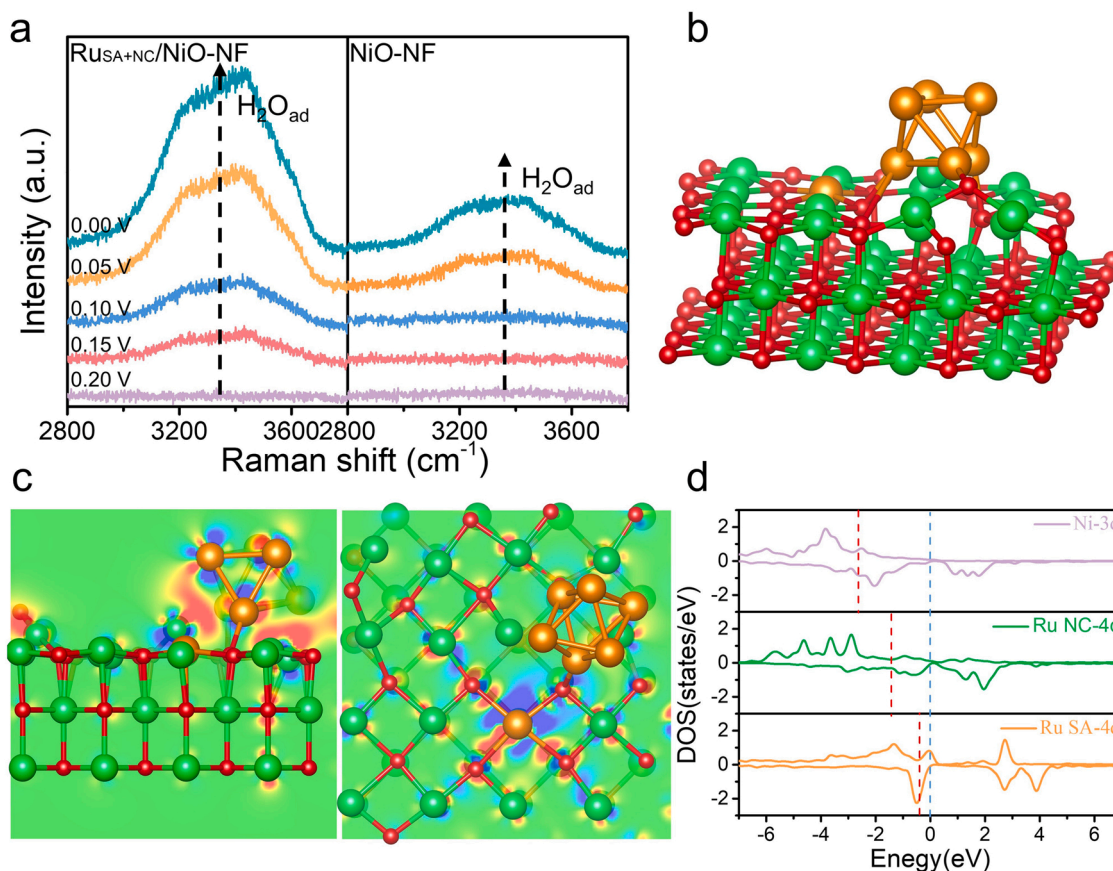


Fig. 4. (a) *In-situ* Raman spectra of the $\text{Ru}_{\text{SA+NC}}/\text{NiO-NF}$ and NiO-NF catalysts collected in the potential range +0.2–0 V. (b) The as-built structural model of the co-existence of Ru single-atoms and Ru nanoclusters doped NiO (denoted as $\text{Ru}_{\text{SA+NC}}/\text{NiO}$). (c) The differential charge density maps of $\text{Ru}_{\text{SA+NC}}/\text{NiO}$. The blue and red colors stand for the loss and acceptance of electrons, respectively. (d) DOS analysis of Ni, Ru nanocluster, and Ru single-atom site in $\text{Ru}_{\text{SA+NC}}/\text{NiO}$.

NF, the in-situ Raman spectroscopy was applied to monitor the capacity for H_2O -adsorption (peak position: $3000\text{--}3600\text{ cm}^{-2}$). H_2O -adsorption is the first step for alkaline HER, which plays an important role in the subsequent H_2O -dissociation and H-recombination. As shown in Fig. 4a, the Raman spectra for $\text{Ru}_{\text{SA}+\text{NC}}/\text{NiO-NF}$ and NiO-NF were carried out among $+0.20\text{--}0.00\text{ V}$ vs RHE. The results indicated that with the decreasing of potential, the peak intensity of H_2O -adsorption increased significantly compared with that of NiO-NF , indicating the $\text{Ru}_{\text{SA}+\text{NC}}/\text{NiO-NF}$ owns a stronger H_2O -adsorption capacity. Therefore, it is reasonable to infer that Ru species are more favorable for the H_2O -adsorption step, which accelerates the following steps for H_2O -dissociation and H-recombination (Fig. 5).

Next, density functional theory (DFT) calculations were also employed to determine the synergistic effect among Ru single-atoms, Ru nanoclusters, and NiO. The model of $\text{Ru}_{\text{SA}+\text{NC}}/\text{NiO}$ was established according to the structural characteristic (Fig. 4b). To explain the origin of the excellent HER performance of $\text{Ru}_{\text{SA}+\text{NC}}/\text{NiO-NF}$, the charge density analysis was first performed to investigate the changes in electronic structure of the catalysts. As shown in Fig. 4c and Fig. S22, the electrons from the Ru single-atom site are partially depleted to the coordinated O sites. Bader charge analysis was executed to further demonstrated the

charge density redistributions and an obvious electron loss on the Ru single-atom site can be achieved (Fig. S23, Supporting Information). The electron-deficient Ru single-atom site is highly active in the adsorption and dissociation of H_2O [25,44]. Next, the density of states (DOS) of the structural model was also calculated. As indicated in Fig. 4d, the d-band center of Ru single-atom is much closer to the Fermi level when compared with that of Ru nanocluster and NiO site. The enriched DOS near the Fermi level improves the conductivity of NiO, as experimentally demonstrated by the reduced charge transfer resistance from EIS (Fig. S24, Supporting Information), further facilitating the HER process [29,42,45–47]. In addition, the increased electron density of Ru single-atom site near Fermi level is responsible for stronger H_2O -adsorption, which is benefit for the following step of H_2O -dissociation [8].

Based on the above, the free energy of intermediates during the HER process was also calculated to elaborate the synergistic effect between Ru single-atoms, Ru nanoclusters, and NiO. For the HER in alkaline medium, the overall pathway can be divided into H_2O -adsorption, H_2O -dissociation, and H-recombination. As shown in Fig. S25–26, H_2O was thermodynamically more favorable adsorption/dissociation on the Ru single-atoms sites (the adsorption energy is -1.12 eV ; the dissociation energy is -2.04 eV) compared with the Ru nanoclusters sites (the

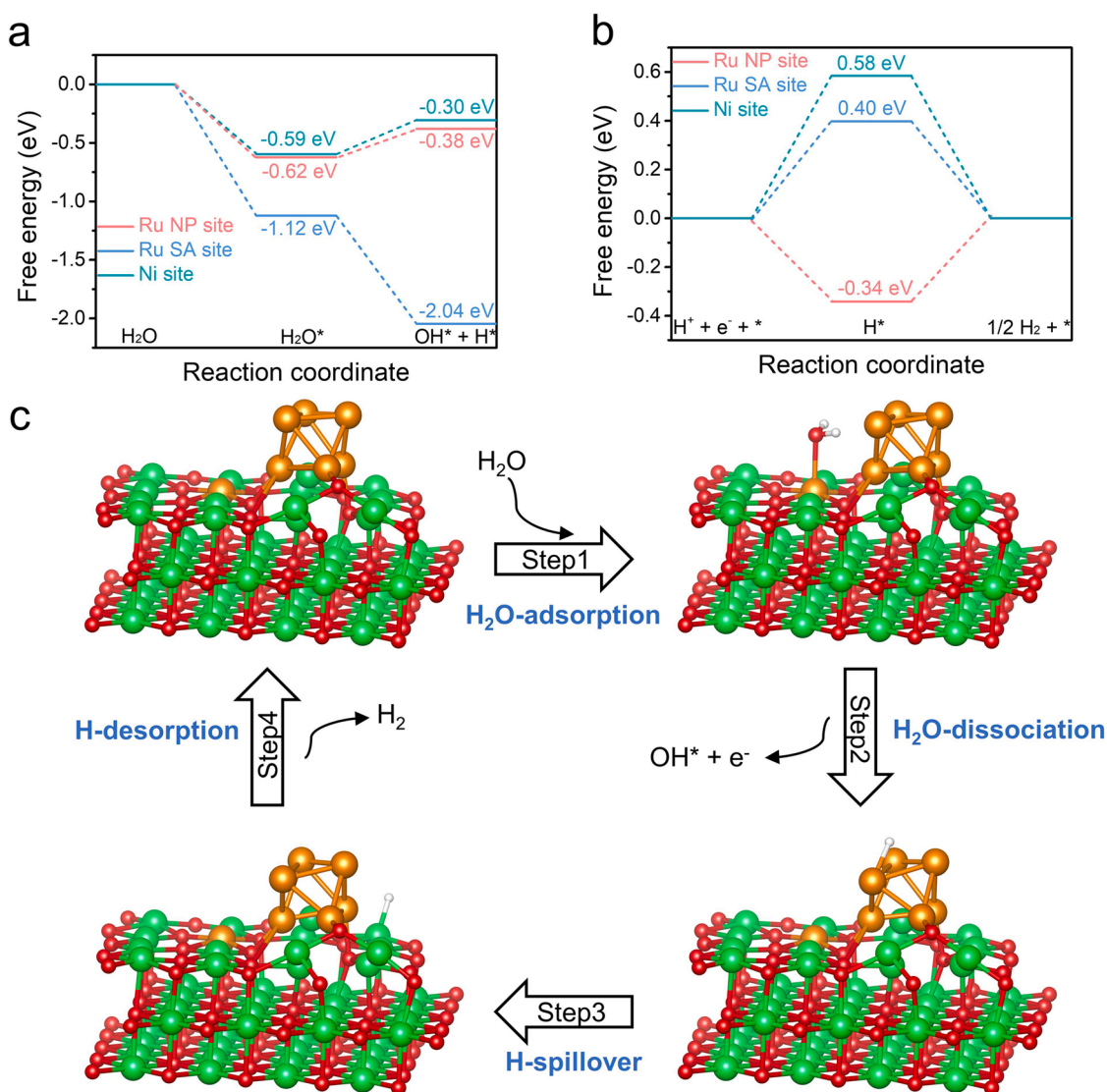


Fig. 5. (a) The free energy diagrams of H_2O adsorption and H_2O -dissociation on different active sites. (b) The free energy diagrams of H-adsorption on different active sites. (c) Schematic illustration of the synergistic effect mechanism among Ru single-atom site, Ru nanocluster site, and NiO site during the alkaline HER process.

adsorption energy is -0.62 eV; the dissociation energy is -0.38 eV) and NiO sites (the adsorption energy is -0.59 eV; the dissociation energy is -0.30 eV). Additionally, the free energy of H-adsorption (ΔG_{H^*}) is also achieved on different active sites. As displayed in Fig. S27, the Ru nanoclusters sites possess a more negative ΔG_{H^*} value (-0.34 eV), indicating the released H prefers to be absorbed on the Ru nanoclusters sites. By contrast, the Ru single-atoms sites ($\Delta G_{H^*} = 0.40$ eV) and NiO sites ($\Delta G_{H^*} = 0.58$ eV) display a weaker attraction to H. Therefore, the H spillover occurs between Ru nanoclusters site (strong H-adsorption on metal) and NiO supporting material (weak H-adsorption on supporting material), and the adsorbed H tends to migrate from Ru nanoclusters site to NiO sites during the hydrogen desorption process.[8,25] According to the calculated adsorption energy and in-situ Raman, a complete set of reaction processes can be considered as below. First, the H_2O molecules preferentially adsorbed and dissociated on the Ru single-atoms sites owing to its lower free energy (Step 1). Then, the hydrolyzate (H species) is expected to move to the Ru nanoclusters sites due to the more negative ΔG_{H^*} value, thus the Ru single-atoms sites can be released to absorb and dissociate next H_2O (Step 2). Eventually, the H species desorbs from the NiO sites via H spillover owing to the weak H-adsorption (Step 3–4). Therefore, when the single-atom/nanoclusters ratio of Ru specie is higher than 0.87 (the ratio for best catalytic activity), the H-adsorption progress is inhibited, while the single-atom/nanoclusters ratio of Ru specie is lower than 0.87, the H-desorption efficiency is limited.[25,48] As such, the $Ru_{SA+NC}/NiO-NF$ achieves a perfect balance among H_2O -adsorption, H_2O -dissociation, and H-recombination, thus realizing ultralow HER overpotential.

5. Conclusion

In summary, a relay catalyst ($Ru_{SA+NC}/NiO-NF$) with three types of active sites (Ru single-atoms, Ru nanoclusters, and NiO) was prepared in this work. Combined with in-situ Raman and DFT calculations, we revealed the synergetic effect among multiple active sites. The results demonstrated that the Ru single-atoms sites exhibited higher activity for H_2O -adsorption and H_2O -dissociation, the Ru nanoclusters sites favored the adsorption of H, and the NiO sites were beneficial to the desorption of H. As such, the as-prepared $Ru_{SA+NC}/NiO-NF$ catalyzed the whole reaction process in the form of relay catalysis, displaying excellent HER activity and high stability in alkaline media. Our work highlighted the designing of composite catalysts with different active sites, where each active site could accelerate one or two steps in the complex reactions. Such a strategy not only improves the limitations of single-atoms catalysts in the catalytic multi-step reaction process but also maximizes their catalytic activity. We anticipate that the idea of designing multiple active sites catalysts will pave a new avenue for designing more efficient electrocatalysts in multi-step catalytic reactions, such as carbon dioxide reduction and oxygen reduction.

CRedit authorship contribution statement

Jiachen Zhang: Methodology, Investigation, Validation, Writing – original draft. **Yanan Gu:** Formal analysis, Methodology. **Yang Lu:** Methodology, Investigation, Conceptualization. **Chengcheng Zhu:** Software. **Guocong Liu:** Software. **Chen Wang:** Visualization, Investigation. **Dongmei Sun:** Writing – review & editing. **Yawen Tang:** Writing – review & editing, Resources. **Hanjun Sun:** Funding, Supervision, Writing – review & editing, Project administration.

Declaration of Competing Interest

The authors declare that they have no known competing financial interests or personal relationships that could have appeared to influence the work reported in this paper.

Data Availability

Data will be made available on request.

Acknowledgment

We acknowledge financial support from the Jiangsu Specially Appointed Professorship, the National Key Research and Development Program of China (2021YFA1502700), the Natural Science Foundation of Jiangsu Province (Grant No. BK 20220369), National Natural Science Foundation of China (22209076, 22232004, 22279062).

Appendix A. Supporting information

Supplementary data associated with this article can be found in the online version at doi:10.1016/j.apcatb.2022.122316.

References

- [1] A.R. Poerwoprajitno, L. Gloag, J. Watt, S. Cheong, X. Tan, H. Lei, H.A. Tahini, A. Henson, B. Subhash, N.M. Bedford, B.K. Miller, P.B. O'Mara, T.M. Benedetti, D. L. Huber, W. Zhang, S.C. Smith, J.J. Gooding, W. Schuhmann, R.D. Tilley, A single-Pt-atom-on-Ru-nanoparticle electrocatalyst for CO-resilient methanol oxidation, *Nat. Catal.* 5 (2022) 231–237.
- [2] L. Liu, A. Corma, Metal Catalysts for Heterogeneous Catalysis: From Single Atoms to Nanoclusters and Nanoparticles, *Chem. Rev.* 118 (2018) 4981–5079.
- [3] J. Wang, W. Fang, Y. Hu, Y. Zhang, J. Dang, Y. Wu, B. Chen, H. Zhao, Z. Li, Single atom Ru doping 2H-MoS₂ as highly efficient hydrogen evolution reaction electrocatalyst in a wide pH range, *Appl. Catal. B: Environ.* 298 (2021), 120490.
- [4] A. Mosallanezhad, C. Wei, P. Ahmadian Koudakan, Y. Fang, S. Niu, Z. Bian, B. Liu, T. Huang, H. Pan, G. Wang, Interfacial synergies between single-atomic Pt and CoS for enhancing hydrogen evolution reaction catalysis, *Appl. Catal. B: Environ.* 315 (2022), 121534.
- [5] J. Zhu, M. Xiao, D. Ren, R. Gao, X. Liu, Z. Zhang, D. Luo, W. Xing, D. Su, A. Yu, Z. Chen, Quasi-Covalently Coupled Ni–Cu Atomic Pair for Synergistic Electroreduction of CO₂, *J. Am. Chem. Soc.* 144 (2022) 9661–9671.
- [6] M. Xiao, Z. Xing, Z. Jin, C. Liu, J. Ge, J. Zhu, Y. Wang, X. Zhao, Z. Chen, Preferentially Engineering FeN₄ Edge Sites onto Graphitic Nanosheets for Highly Active and Durable Oxygen Electrocatalysis in Rechargeable Zn–Air Batteries, *Adv. Mater.* 32 (2020), 2004900.
- [7] K. Jiang, M. Luo, Z. Liu, M. Peng, D. Chen, Y.R. Lu, T.S. Chan, F.M.F. de Groot, Y. Tan, Rational strain engineering of single-atom ruthenium on nanoporous MoS₂ for highly efficient hydrogen evolution, *Nat. Commun.* 12 (2021) 1687.
- [8] D. Cao, J. Wang, H. Xu, D. Cheng, Construction of Dual-Site Atomically Dispersed Electrocatalysts with Ru–C₅ Single Atoms and Ru–O₂ Nanoclusters for Accelerated Alkali Hydrogen Evolution, *Small* 17 (2021), e2101163.
- [9] F. Cheng, L. Wang, H. Wang, C. Lei, B. Yang, Z. Li, Q. Zhang, L. Lei, S. Wang, Y. Hou, Boosting alkaline hydrogen evolution and Zn–H₂O cell induced by interfacial electron transfer, *Nano Energy* 71 (2020), 104621.
- [10] C. Lei, Y. Wang, Y. Hou, P. Liu, J. Yang, T. Zhang, X. Zhuang, M. Chen, B. Yang, L. Cui, C. Yuan, M. Qiu, X. Feng, Efficient alkaline hydrogen evolution on atomically dispersed Ni–N_x Species anchored porous carbon with embedded Ni nanoparticles by accelerating water dissociation kinetics, *Energy Environ. Sci.* 12 (2019) 149–156.
- [11] Q. Dai, L. Wang, K. Wang, X. Sang, Z. Li, B. Yang, J. Chen, L. Lei, L. Dai, Y. Hou, Accelerated Water Dissociation Kinetics by Electron-Enriched Cobalt Sites for Efficient Alkaline Hydrogen Evolution, *Adv. Funct. Mater.* 32 (2022), 2109556.
- [12] X. Duan, P. Li, D. Zhou, S. Wang, H. Liu, Z. Wang, X. Zhang, G. Yang, Z. Zhang, G. Tan, Y. Li, L. Xu, W. Liu, Z. Xing, Y. Kuang, X. Sun, Stabilizing single-atomic ruthenium by ferrous ion doped NiFe-LDH towards highly efficient and sustained water oxidation, *Chem. Eng. J.* 446 (2022), 136962.
- [13] C.H. Chen, D. Wu, Z. Li, R. Zhang, C.G. Kuai, X.R. Zhao, C.K. Dong, S.Z. Qiao, H. Liu, X.W. Du, Ruthenium-Based Single-Atom Alloy with High Electrocatalytic Activity for Hydrogen Evolution, *Adv. Energy Mater.* 9 (2019), 1803913.
- [14] B. Mao, P. Sun, Y. Jiang, T. Meng, D. Guo, J. Qin, M. Cao, Identifying the Transfer Kinetics of Adsorbed Hydroxyl as a Descriptor of Alkaline Hydrogen Evolution Reaction, *Angew. Chem. Int. Ed.* 59 (2020) 15232–15237.
- [15] N. Yao, R. Meng, F. Wu, Z. Fan, G. Cheng, W. Luo, Oxygen-Vacancy-Induced CeO₂/Co₄N heterostructures toward enhanced pH-Universal hydrogen evolution reactions, *Appl. Catal. B: Environ.* 277 (2020), 119282.
- [16] X. Fan, C. Liu, M. Wu, B. Gao, L. Zheng, Y. Zhang, H. Zhang, Q. Gao, X. Cao, Y. Tang, Synergistic effect of dual active sites over Ru/α-MoC for accelerating alkaline hydrogen evolution reaction, *Appl. Catal. B: Environ.* 318 (2022), 121867.
- [17] J. Zhu, S. Li, M. Xiao, X. Zhao, G. Li, Z. Bai, M. Li, Y. Hu, R. Feng, W. Liu, R. Gao, D. Su, A. Yu, Z. Chen, Tensile-strained ruthenium phosphide by anion substitution for highly active and durable hydrogen evolution, *Nano Energy* 77 (2020), 105212.
- [18] C. Wang, K. Wang, Y. Feng, C. Li, X. Zhou, L. Gan, Y. Feng, H. Zhou, B. Zhang, X. Qu, H. Li, J. Li, A. Li, Y. Sun, S. Zhang, G. Yang, Y. Guo, S. Yang, T. Zhou, F. Dong, K. Zheng, L. Wang, J. Huang, Z. Zhang, X. Han, Co and Pt Dual-Single-

- Atoms with Oxygen-Coordinated Co-O-Pt Dimer Sites for Ultrahigh Photocatalytic Hydrogen Evolution Efficiency, *Adv. Mater.* 33 (2021), e2003327.
- [19] Z. Zheng, L. Yu, M. Gao, X. Chen, W. Zhou, C. Ma, L. Wu, J. Zhu, X. Meng, J. Hu, Y. Tu, S. Wu, J. Mao, Z. Tian, D. Deng, Boosting hydrogen evolution on MoS₂ via co-confining selenium in surface and cobalt in inner layer, *Nat. Commun.* 11 (2020) 3315.
 - [20] H. Song, M. Wu, Z. Tang, J.S. Tse, B. Yang, S. Lu, Single Atom Ruthenium-Doped CoP/CDs Nanosheets via Splicing of Carbon-Dots for Robust Hydrogen Production, *Angew. Chem. Int. Ed.* 60 (2021) 7234–7244.
 - [21] K.L. Zhou, Z. Wang, C.B. Han, X. Ke, C. Wang, Y. Jin, Q. Zhang, J. Liu, H. Wang, H. Yan, Platinum single-atom catalyst coupled with transition metal/metal oxide heterostructure for accelerating alkaline hydrogen evolution reaction, *Nat. Commun.* 12 (2021) 3783.
 - [22] G. Chen, T. Wang, J. Zhang, P. Liu, H. Sun, X. Zhuang, M. Chen, X. Feng, Accelerated Hydrogen Evolution Kinetics on NiFe-Layered Double Hydroxide Electrocatalysts by Tailoring Water Dissociation Active Sites, *Adv. Mater.* 30 (2018), 1706279.
 - [23] X. Wu, Z. Wang, D. Zhang, Y. Qin, M. Wang, Y. Han, T. Zhan, B. Yang, S. Li, J. Lai, L. Wang, Solvent-free microwave synthesis of ultra-small Ru-Mo₂C@CNT with strong metal-support interaction for industrial hydrogen evolution, *Nat. Commun.* 12 (2021) 4018.
 - [24] J. Zhang, G. Chen, Q. Liu, C. Fan, D. Sun, Y. Tang, H. Sun, X. Feng, Competitive Adsorption: Reducing the Poisoning Effect of Adsorbed Hydroxyl on Ru Single-Atom Site with SnO₂ for Efficient Hydrogen, *Evol., Angew. Chem. Int. Ed.* 61 (2022), e202209486.
 - [25] M. Lao, G. Zhao, P. Li, T. Ma, Y. Jiang, H. Pan, S.X. Dou, W. Sun, Manipulating the Coordination Chemistry of Ru-N(O)-C Moieties for Fast Alkaline Hydrogen Evolution Kinetics, *Adv. Funct. Mater.* 31 (2021), 2100698.
 - [26] Z.H. Ibupoto, A. Tahir, P. Tang, X. Liu, J.R. Morante, M. Fahlman, J. Arbiol, M. Vagin, A. Vomiero, MoS_x@NiO Composite Nanostructures: An Advanced Nonprecious Catalyst for Hydrogen Evolution Reaction in Alkaline Media, *Adv. Funct. Mater.* 29 (2019), 1807562.
 - [27] Z. Zhang, C. Feng, C. Liu, M. Zuo, L. Qin, X. Yan, Y. Xing, H. Li, R. Si, S. Zhou, J. Zeng, Electrochemical deposition as a universal route for fabricating single-atom catalysts, *Nat. Commun.* 11 (2020) 1215.
 - [28] P. Su, W. Pei, X. Wang, Y. Ma, Q. Jiang, J. Liang, S. Zhou, J. Zhao, J. Liu, G.Q. M. Lu, Exceptional Electrochemical HER Performance with Enhanced Electron Transfer between Ru Nanoparticles and Single Atoms Dispersed on a Carbon Substrate, *Angew. Chem. Int. Ed.* 60 (2021) 16044–16050.
 - [29] Q. He, Y. Zhou, H. Shou, X. Wang, P. Zhang, W. Xu, S. Qiao, C. Wu, H. Liu, D. Liu, S. Chen, R. Long, Z. Qi, X. Wu, L. Song, Synergic Reaction Kinetics over Adjacent Ruthenium Sites for Superb Hydrogen Generation in Alkaline Media, *Adv. Mater.* 34 (2022), e2110604.
 - [30] P. Li, M. Wang, X. Duan, L. Zheng, X. Cheng, Y. Zhang, Y. Kuang, Y. Li, Q. Ma, Z. Feng, W. Liu, X. Sun, Boosting oxygen evolution of single-atomic ruthenium through electronic coupling with cobalt-iron layered double hydroxides, *Nat. Commun.* 10 (2019) 1711.
 - [31] T.Y. Chen, G.W. Lee, Y.T. Liu, Y.F. Liao, C.C. Huang, D.S. Lin, T.L. Lin, Heterojunction confinement on the atomic structure evolution of near monolayer core-shell nanocatalysts in redox reactions of a direct methanol fuel cell, *J. Mater. Chem. A* 3 (2015) 1518–1529.
 - [32] J. Kim, P.C. Shih, K.C. Tsao, Y.T. Pan, X. Yin, C.J. Sun, H. Yang, High-Performance Pyrochlore-Type Yttrium Ruthenate Electrocatalyst for Oxygen Evolution Reaction in Acidic Media, *J. Am. Chem. Soc.* 139 (2017) 12076–12083.
 - [33] Z. Zhao, H. Liu, W. Gao, W. Xue, Z. Liu, J. Huang, X. Pan, Y. Huang, Surface-Engineered PtNi-O Nanostructure with Record-High Performance for Electrocatalytic Hydrogen Evolution Reaction, *J. Am. Chem. Soc.* 140 (2018) 9046–9050.
 - [34] S. Liu, Y. Shen, Y. Zhang, B. Cui, S. Xi, J. Zhang, L. Xu, S. Zhu, Y. Chen, Y. Deng, W. Hu, Extreme Environmental Thermal Shock Induced Dislocation-Rich Pt Nanoparticles Boosting Hydrogen Evolution Reaction, *Adv. Mater.* 34 (2022), e2106973.
 - [35] W. Li, Y. Zhao, Y. Liu, M. Sun, G.I.N. Waterhouse, B. Huang, K. Zhang, T. Zhang, S. Lu, Exploiting Ru-Induced Lattice Strain in CoRu Nanoalloys for Robust Bifunctional Hydrogen Production, *Angew. Chem. Int. Ed.* 60 (2021) 3290–3298.
 - [36] Y. Sun, Z. Xue, Q. Liu, Y. Jia, Y. Li, K. Liu, Y. Lin, M. Liu, G. Li, C.Y. Su, Modulating electronic structure of metal-organic frameworks by introducing atomically dispersed Ru for efficient hydrogen evolution, *Nat. Commun.* 12 (2021) 1369.
 - [37] T. Kou, M. Chen, F. Wu, T.J. Smart, S. Wang, Y. Wu, Y. Zhang, S. Li, S. Lall, Z. Zhang, Y.S. Liu, J. Guo, G. Wang, Y. Ping, Y. Li, Carbon doping switching on the hydrogen adsorption activity of NiO for hydrogen evolution reaction, *Nat. Commun.* 11 (2020) 590.
 - [38] L. Zhao, Y. Zhang, Z. Zhao, Q.H. Zhang, L.B. Huang, L. Gu, G. Lu, J.S. Hu, L.J. Wan, Steering elementary steps towards efficient alkaline hydrogen evolution via size-dependent Ni/NiO nanoscale heterosurfaces, *Natl. Sci. Rev.* 7 (2020) 27–36.
 - [39] D.H. Kwon, M.S. Okyay, S.J. Kim, J.P. Jeon, H.J. Noh, N. Park, J. Mahmood, J. B. Baek, Ruthenium anchored on carbon nanotube electrocatalyst for hydrogen production with enhanced Faradaic efficiency, *Nat. Commun.* 11 (2020) 1278.
 - [40] C. Cai, K. Liu, Y. Zhu, P. Li, Q. Wang, B. Liu, S. Chen, H. Li, L. Zhu, H. Li, J. Fu, Y. Chen, E. Pensa, J. Hu, Y.R. Lu, T.S. Chan, E. Cortes, M. Liu, Optimizing Hydrogen Binding on Ru Sites with RuCo Alloy Nanosheets for Efficient Alkaline Hydrogen Evolution, *Angew. Chem. Int. Ed.* 61 (2022), e202113664.
 - [41] H. Sun, C.W. Tung, Y. Qiu, W. Zhang, Q. Wang, Z. Li, J. Tang, H.C. Chen, C. Wang, H.M. Chen, Atomic Metal-Support Interaction Enables Reconstruction-Free Dual-Site Electrocatalyst, *J. Am. Chem. Soc.* 144 (2022) 1174–1186.
 - [42] P. Zhai, M. Xia, Y. Wu, G. Zhang, J. Gao, B. Zhang, S. Cao, Y. Zhang, Z. Li, Z. Fan, C. Wang, X. Zhang, J.T. Miller, L. Sun, J. Hou, Engineering single-atomic ruthenium catalytic sites on defective nickel-iron layered double hydroxide for overall water splitting, *Nat. Commun.* 12 (2021) 4587.
 - [43] Z. Cheng, Y. Xiao, W. Wu, X. Zhang, Q. Fu, Y. Zhao, L. Qu, All-pH-Tolerant In-Plane Heterostructures for Efficient Hydrogen Evolution Reaction, *ACS Nano* 15 (2021) 11417–11427.
 - [44] C. Li, H. Jang, M.G. Kim, L. Hou, X. Liu, J. Cho, Ru-incorporated oxygen-vacancy-enriched MoO₃ electrocatalysts for hydrogen evolution reaction, *Appl. Catal. B: Environ.* 307 (2022), 121204.
 - [45] Q. He, D. Tian, H. Jiang, D. Cao, S. Wei, D. Liu, P. Song, Y. Lin, L. Song, Achieving Efficient Alkaline Hydrogen Evolution Reaction over a Ni₅P₄ Catalyst Incorporating Single-Atomic Ru Sites, *Adv. Mater.* 32 (2020), e1906972.
 - [46] X. Chen, J. Wan, J. Wang, Q. Zhang, L. Gu, L. Zheng, N. Wang, R. Yu, Atomically Dispersed Ruthenium on Nickel Hydroxide Ultrathin Nanoribbons for Highly Efficient Hydrogen Evolution Reaction in Alkaline Media, *Adv. Mater.* 33 (2021), e2104764.
 - [47] J. Luo, J. Wang, Y. Guo, J. Zhu, H. Jin, Z. Zhang, D. Zhang, Y. Niu, S. Hou, J. Du, D. He, Y. Xiong, L. Chen, S. Mu, Y. Huang, Metal-organic frameworks derived RuP₂ with yolk-shell structure and efficient performance for hydrogen evolution reaction in both acidic and alkaline media, *Appl. Catal. B: Environ.* 305 (2022), 121043.
 - [48] J. Li, J. Hu, M. Zhang, W. Gou, S. Zhang, Z. Chen, Y. Qu, Y. Ma, A fundamental viewpoint on the hydrogen spillover phenomenon of electrocatalytic hydrogen evolution, *Nat. Commun.* 12 (2021) 3502.